

Nucleation Dynamics for Water Condensation on Lubricant-Infused Surfaces

Jianxing Sun^a, Vivek V. Manepalli^{a,b}, Patricia B. Weisensee^{a,c,*}

a. Department of Mechanical Engineering & Materials Science, Washington University in St. Louis, USA

b. Department of Mechanical Engineering, Birla Institute of Technology & Science, Pilani – Hyderabad, India

c. Institute of Materials Science and Engineering, Washington University in St. Louis, USA

* corresponding author: p.weisensee@wustl.edu

Abstract In recent decades, various non-wettable surfaces have been proposed to promote dropwise condensation, featuring much higher heat transfer rates than traditional filmwise condensation. Lubricant-infused surfaces (LIS or SPLIPS) can promote stable dropwise condensation and improve heat transfer rates due to a low nucleation energy barrier and high droplet mobility, leading to high sweeping and re-nucleation rates. However, the nucleation dynamics on lubricant-infused surfaces are considerably less studied and the interplay between the lubricant film and nucleation has been a matter of intense debate. In this work, we conduct water vapor condensation experiments on LIS infused with Krytox oil of varying viscosity within a custom-design chamber with controllable vapor temperature at atmospheric pressure. Using high-speed optical and infrared imaging and optical microscopy, we show that nucleation predominantly occurs in the oil-poor regions where the oil-vapor interfacial temperature is lower than in oil-rich regions. This small temperature difference causes an order magnitude lower free-energy nucleation barrier, leading to enhanced nucleation. The relative area ratio of oil-poor regions to total surface area, *i.e.*, preferred area for nucleation, can be tailored between 11% and 19% by changing the lubricant viscosity from 1627 to 73 cP. We statistically analyze the influence of lubricant viscosity on the new emerging droplets on LIS at a broad range of vapor supersaturation ratios. The results show that the nucleation rate density dramatically increases with vapor supersaturation. More importantly, a strong dependence of nucleation rate density on lubricant viscosity exists in the whole range of supersaturation ratios, which means that higher heat transfer rates can potentially be achieved by lowering lubricant viscosity.

Keywords Lubricant-infused surface; LIS; Dropwise condensation; Nucleation rate; Nucleation density

Introduction

Achieving dropwise condensation is of continued interest and desirable in many industrial applications, such as water-harvesting [1], desalination [2,3], power generation [4], and thermal management [5], due to higher heat transfer performance and water collection rates. In recent decades, many efforts have been dedicated to creating various non-wettable engineered surfaces, *e.g.* superhydrophobic [6,7], hybrid [8], and lubricant-infused surfaces (LIS or SPLIPS) [9], to enable the formation of discrete condensate droplets and to enhance water shedding from the surface once condensed. Notably, LIS can promote stable dropwise condensation of water and low surface energy liquids [10,11]. As we have shown previously, condensed droplets can also robustly self-propel during condensation caused by the overlap of oil menisci surrounding water droplets, continuously refreshing nucleation sites on the surface [12]. The droplets can depart from substrates at relatively smaller critical diameter under gravity due to their extremely low contact angle hysteresis. At the same time, onset of heterogeneous water nucleation intrinsically occurs more easily on a soft or liquid surface than a solid one under the same conditions. Many researchers have shown through theoretical modeling that the energy barrier for heterogeneous nucleation on a fluid surface is lower than on a rigid surface based on a Gibbsian thermodynamic surface analysis [13,14]. Sokuler and co-workers experimentally investigated the nucleation and the growth of condensing water drops on soft poly(dimethyl siloxane) (PDMS) films with varying elasticity and viscosity. They found that nucleation is faster on a soft surface than on a hard one due to a reduced activation barrier for nucleation [15]. All of these benefits can potentially improve nucleation and thereby significantly enhance the heat transfer performance on LIS [16–18], since microscopic condensate droplets ($< 10 \mu\text{m}$) account for approximately 75% of the total heat transfer during dropwise condensation [19].

In spite of its importance, the exact mechanism for droplet nucleation on LIS remains elusive. On a solid surface, droplets are thought to nucleate primarily on topographical and chemical defects, such as cavities and hydrophilic sites [20,21], and grow by direct vapor diffusion and coalescence with other droplets. However, nucleation dynamics on LIS are fundamentally unique due to the existence of a layer of a molecularly smooth lubricant film between water vapor and the solid superhydrophobic surface. This layer of lubricant film potentially facilitates water nucleation. However, the preferred location for nucleation remains a matter of intense debate. Xiao *et al.* assumed that vapor diffuses through a thin layer of lubricant covering hydrophilic sites of bi-philic pillars and nucleates at the lubricant-solid interface [16]. Anand *et al.* argued, based on theoretical considerations of vapor transport in liquids, that – while thermodynamically (*i.e.*, at equilibrium) favorable – nucleation at the lubricant-solid interface is not likely due to the limited solubility of vapor in the lubricant. They proposed that droplets nucleate at the lubricant-vapor interface, and later move into the lubricant due to cloaking and capillary forces [22] and supported their hypothesis with cryogenic focused ion beam SEM (cryo-FIB-SEM) images. Using 3D laser scanning confocal microscopy, Kajiya *et al.* confirmed that droplets nucleate at the lubricant-vapor interface, preferentially at the edges of pillars, where the lubricant curvature decreases the energy barrier for nucleation. After subsequent coalescence, droplets migrate to the space between pillars and grow to the bottom of the lubricant layer [23]. In the process of condensation, the dynamic lubricant film will be pulled up and form menisci surrounding condensate droplets due to capillary forces. Our previous studies have shown that the thin lubricant film redistributes into oil-rich and oil-poor regions and continuously re-distributes [12]. The varying oil thickness is expected to potentially influence the spatial preference of nucleation due to varying thermal resistances in the oil-rich and oil-poor regions. Hence, fundamental questions pertaining to nucleation and growth of droplets on LIS with a layer of a dynamic liquid film need to be investigated. Macroscopically, the distribution of droplet sizes on LIS has been reported to be independent of lubricant viscosity [19], however, lower viscosity oil-infused smooth surfaces showed a higher condensation heat

transfer coefficient than those with oil of higher viscosity [24]. We hypothesize that the lubricant viscosity and the associated droplet mobility influence droplet nucleation. The values of droplet density, that is, the first generation of nucleation density reported by most studies on dropwise condensation are likely not suited to accurately reflect long-term average nucleation and heat transfer during condensation. To better evaluate condensation and heat transfer rates, we propose that it is necessary to examine the transient (re-)nucleation density during longer time intervals, and introduce the concept of a nucleation rate density, which takes into account the area available for re-nucleation (*i.e.*, a spatial component), and kinetics of nucleation (*i.e.*, a temporal component).

In this paper, in order to experimentally examine the interplay of lubricant dynamics and nucleation during condensation, we conducted water vapor condensation experiments in the presence of non-condensable gases on Krytox lubricant-infused surfaces in a custom-designed environmental chamber with controllable vapor and substrate temperatures at atmosphere pressure. The spatial distribution of preferential nucleation was investigated using high-speed imaging and optical microscopy. The area ratio of oil-poor regions, *i.e.* the favorable area for nucleation, to the total surface area on LIS was analyzed at different times during condensation. We also examined the dependence of the formation and area of oil-poor regions on lubricant viscosity. Finally, we conducted condensation experiments on LIS with different lubricant viscosities at a wide range of subcooling degrees (or supersaturation ratios). The average nucleation rate density ($\#/m^2 \cdot s$) in a complete condensation cycle is presented to demonstrate the overall nucleation and condensation process. We conducted a statistical analysis over many such cycles to elucidate the relationship between nucleation rate density, lubricant viscosity, and supersaturation. The temperature distribution of the oil-vapor interface on LIS during condensation is characterized using infrared imaging to interpret nucleation on LIS. These findings will advance our understanding of the mechanism of droplet nucleation on LIS, and help inform the selection of a lubricant for LIS to achieve higher nucleation rate densities and condensation heat transfer rates.

2 Materials and methods

2.1 Preparation of lubricant-infused surfaces

The substrate was obtained by cutting a plain microscope glass slide (Thermo Scientific) into pieces (25 cm \times 25 cm), then rinsed with acetone, isopropanol, and de-ionized (DI) water in sequence, and dried with compressed N₂. Subsequently, the cleaned glass surface was sprayed with a layer of commercially available superhydrophobic agent (Glaco Mirror Coat, soft 99 Co.), and placed in the fume hood for one hour to ensure complete solvent evaporation. A layer of relatively uniform nanostructure was created, as shown in the inserted images of **Figure 1**. In this work, Krytox GPL oils were chosen as the infused liquid, featuring very different viscosities but similar surface tensions of $\gamma_{ov} = 17 \pm 1$ mN/m in vapor and $\gamma_{do} = 53$ mN/m in water [25]. To obtain the lubricant-infused surface, the nanostructured surface was impregnated with Krytox oils *via* spin coating. Based on the spin coating model developed by Emslie [26], the film thickness scales as $d_{oil} \sim (\mu/t\omega^2)^{1/2}$, where μ is the oil viscosity, t is the total rotating time of the sample, and ω is the angular velocity of the sample. Here, the thickness of the initial oil film was approximately 15 μ m for the different viscosity oils by adjusting the revolutions per minute (RPM), as shown in **Table 1**. For a millimetric water droplet, the apparent contact angle on LIS is approximately 90°. Microscopically, Krytox GPL series oils cloak water, *i.e.*, spread on the condensed water droplets and the superhydrophobic sample due to positive spreading coefficients [27–29]: $S_{do(v)} = \gamma_{dv} - \gamma_{ov} - \gamma_{do} > 0$ and $S_{os(d)} = \gamma_{ds} - \gamma_{os} - \gamma_{do} > 0$, where γ_{dv} , γ_{ov} , γ_{do} , γ_{os} and γ_{ds} denote the interfacial energies between water droplet-vapor, oil-vapor, water droplet-oil, oil-solid and water droplet-solid, respectively.[30,31] For comparison, hydrophobic samples were also

prepared by coating the cleaned glass with a layer of hexadecyltrimethoxysilane (HTMS) with a static contact angle around 95° .

2.2 Water vapor condensation experiments

We conducted water vapor condensation experiments on horizontally placed LIS with varying lubricant viscosity at a series of supersaturation ratios (SRs) in a custom-designed chamber. The supersaturation ratio is defined as:

$$SR = \frac{P_v \times RH(\%) - P_{v,sat}}{P_{v,sat}}, \quad (1)$$

where P_v and RH are the vapor partial pressure and relative humidity of bulk vapor in the chamber, and $P_{v,sat}$ is the saturated vapor pressure at the substrate surface. As shown in [Figure 1](#), a LIS sample was placed on a copper block inside the chamber. A cold plate connected to the copper block was maintained at a constant temperature ($T_s \approx 276$ K) by the circulation of ice water. A flask containing DI-water was heated on a hot plate. Compressed nitrogen gas was supplied to the bottom of the flask at a flow rate of 12.5 liters per minute (LPM) and then hot water vapor mixed with N_2 was guided into the chamber by insulated plastic tubes. The temperature and relative humidity (RH) in the chamber were monitored by an RH probe (PCMini52, MICHELL Instruments) with an accuracy of ± 1 K and 1% at $RH = 20\% - 90\%$, respectively. The nucleation dynamics were monitored under an upright DIY Cerna Microscope (Thorlabs) equipped with brightfield objectives (10 \times , 50 \times , 100 \times L Plan SLWD). Videos were obtained using a Photron FASTCAM Mini AX200 high-speed camera at 250 or higher frames per second (fps).

Table 1 Physical properties and corresponding spin coating parameters

Lubricant	Viscosity [cP]	Surface Tension γ_{ov} [mN/m] [25]	RPM	Time [s]
Krytox GPL102	73	17 \pm 1	600	120
Krytox GPL 104	350	17 \pm 1	1160	120
Krytox GPL106	1627	17 \pm 1	2700	120

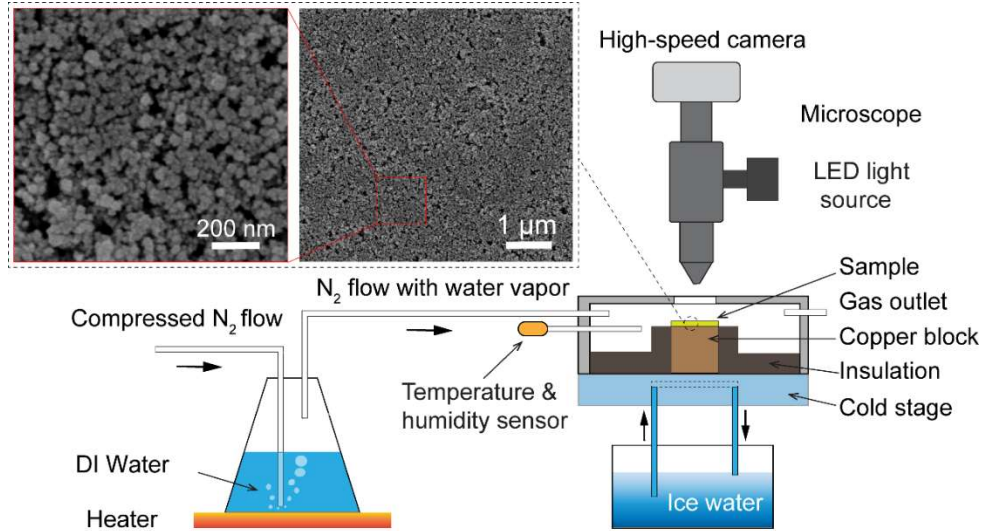


Figure. 1 Schematic of the experimental set-up. Scanning electron microscope (SEM) images show the nanostructured superhydrophobic prior to oil infusion.

2.3 Image processing for identifying oil-poor regions

To obtain the initial re-distribution and information on the area-ratio of oil-poor regions, we conducted experiments with low magnification (10×) at 250 fps. We then extracted one frame of the videos every 5 seconds to perform a detailed image analysis. Image sequences were first processed by MATLAB to eliminate any unevenness of illumination and to improve image quality. Then, the corrected image sequences in grayscales were cropped into 500×500 pixels (0.86 mm^2), as shown in [Figure 2a](#). The gray value is inversely proportional to oil film thickness, as less light is absorbed and scattered by the thinner oil layer. [Figure 2b](#) shows the change of grayscale values along the cyan line in [Figure 2a](#). The grayscale values between points B and C are uniformly high, corresponding to oil-poor regions. However, the value decreases between points B and A, since an oil meniscus with an exponential height profile surrounds the droplet. We define this region as oil-rich. By adjusting the threshold of the grayscale for each video separately to the value of point B in ImageJ, the image sequences are converted into binary images: black for oil-poor regions and white for oil-rich regions and droplets, as seen in [Figure 2c](#). The bright spots in the center of droplets were removed by an image segmentation process. Finally, we used the particle analysis function in ImageJ to calculate the total area of black patches in each frame and relate it to the total area to obtain the ratio of oil-poor regions. This area fraction is calculated for a minimum of 17 different samples of the same lubricant and averaged so that the final values converge to a mean value and reduce error.

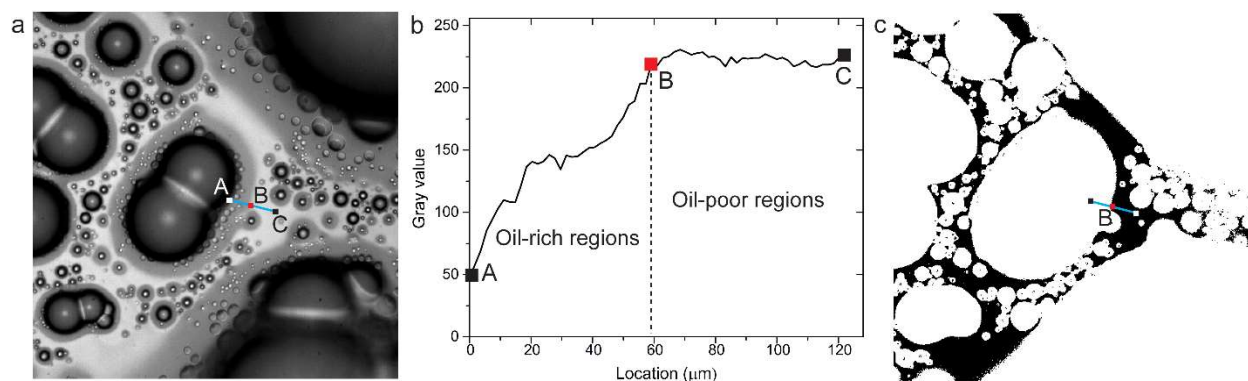


Figure 2 (a) A grayscale image of condensation and oil re-distribution on LIS. The cyan color line spans oil-rich regions (point A) to oil-poor regions (point C). Point B marks the transition point between the two regions. (b) Grayscale values of the line A-B-C in (a). (c) The binary image after applying the grayscale threshold from point B to image (a).

2.4 Statistical analysis of nucleation rate density

New samples were used for each experiment with a certain combination of lubricant viscosity and SR, and every experiment was repeated at least three times. We recorded three sweeping cycles for each sample with a 50 \times objective lens and observed 5 – 7 locations in each sweep. At each location, one video was recorded with a duration of about 12 seconds. Three randomly selected one-second long segments were extracted from each video and the number of nucleation events were counted manually at every frame. The size of the region of interest was 900 \times 950 pixels, that is, 0.117 mm² for the 50 \times objective. Additional data point analysis was adopted when existing data showed a big deviation. Finally, we averaged the results from every data point within different sweeping cycles for each combination of lubricant viscosity and SR. It is extremely challenging to experimentally characterize the nucleation rate density, since the nucleation process originates at a molecular scale with cluster sizes of a few nanometers. Here, we counted the number of nucleated droplets once they became visible. The smallest detectable droplet is $1.85 \pm 0.37 \mu\text{m}$. Using the 100 \times objective lens, we were able to detect droplets with approximately 1 μm diameter and observed that droplets smaller than 2 μm rarely coalesce with neighboring droplets. Therefore, it is safe to use the 50 \times objective to increase the field of view at the expense of resolution and approximate the number of the smallest microdroplets to be representative of the number of nucleating droplets. We also acknowledge that nucleation might be undercounted due to sweeping of big droplets on the surface before nucleation becomes visible with our method. However, this difference is nearly negligible for high viscous lubricants due to a lower mobility of droplets. To a certain extent, our results will underestimate the real nucleation rate density, however, are well suited to elucidate the general effect of lubricant viscosity on nucleation and condensation dynamics.

3. Results and discussion

3.1 Preferred areas for nucleation: oil-poor regions

Due to limited vapor diffusion in an oil film as well as the low nucleation energy barrier of the lubricant-air interface, water nucleation has been assumed to happen on the oil-vapor interface of LIS [13,27] as schematically shown in [Figure 3a](#). Subsequently, the droplets move into the lubricant due to oil cloaking and capillary forces. Based on our previous study, however, the initial uniform layer of lubricant film

redistributes after the first generation of nucleation and growth of water droplets, leading to the formation of oil-rich and oil-poor regions [12]. One question that naturally arises is whether the dynamic lubricant film affects the spatial preference of water nucleation. At the beginning of the condensation process, a first generation of spatially uniform nucleation will occur on the flat oil-vapor interface of a LIS. Then, the oil film starts to redistribute due to droplet growth and movement for the remainder of the condensation process. Oil-rich and oil-poor regions simultaneously occur and dynamically change. A detailed description of oil film re-distribution can be found in our previous work [12]. To investigate the interplay of nucleation and the dynamic oil film during condensation, here we conducted condensation experiments on LIS with Krytox GPL 104 in the custom-designed chamber in the presence of a non-condensable carrier gas N_2 . In the optical image sequence of **Figures 3b, c**, oil-poor regions (marked with red ellipses) are characterized by having a brighter color, as less light is absorbed and scattered by the thin oil layer compared to a thicker one, and wide interference fringes. At $t = 0.24$ s, the image shows nucleation is limited to occur in the oil-poor regions, and droplets coalesce with neighboring ones to create new oil-poor regions. **Figure 3c** presents a relatively larger view of a characteristic condensation process with help of the 20 \times objective. To obtain these two images, we conducted a condensation experiment to generate the non-uniform oil distribution. Then, condensation was halted by shutting off the supply of hot vapor and coolant circulation, and microdroplets in oil-poor regions were removed by evaporation or self-propulsion towards big droplets. Extra caution is needed to prevent evaporation of larger droplets sitting in the center of oil-rich regions. Then, we switched on the coolant and hot vapor in sequence. The emergence of condensation nuclei on the sample surface was imaged using the high-speed camera at 500 fps to capture the first emerging droplets. We see that nucleation (circled in yellow by ImageJ) is confined to the oil-poor regions.

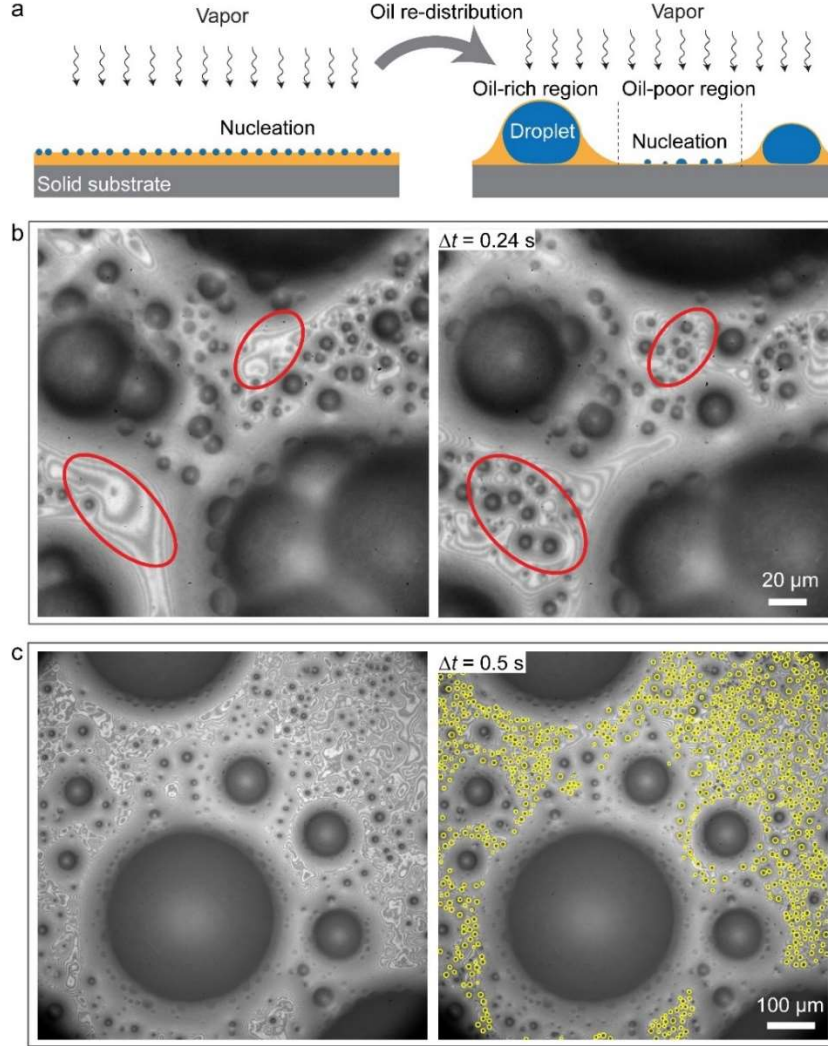


Figure 3 (a) Schematics of nucleation at the beginning of condensation and after the oil film re-distribution process on LIS. Subsequent generations of nucleation mainly occur in the oil-poor regions. (b) & (c) Optical imaging sequences of nucleation on a LIS with Krytox GPL 104 at the magnification of (b) 50 \times and (c) 20 \times . Oil-poor regions are marked with red ellipses in (b). Yellow circles in (c) highlight nucleated droplets.

We can explain the preferred nucleation in the oil-poor region by combining conduction heat transfer analysis and classical nucleation theory. The insert of [Figure 4a](#) shows that a lower conduction resistance R_{oil} of the oil film is expected in the oil-poor regions due to a thinner layer of oil. According to Fourier's Law, we can consider the heat transfer in the oil film as one-dimensional conduction from the oil-vapor interface (temperature T_{ov}) to the colder oil-solid interface (temperature T_s):

$$q'' = k_{oil} \cdot \frac{T_{ov} - T_s}{d_{oil}}, \quad (2)$$

where q'' is the heat flux, k_{oil} the thermal conductivity of the oil, and d_{oil} the local thickness of the oil. Assuming a heat flux of $q'' = 100 \text{ kw/m}^2$ and $T_s = 276 \text{ K}$, [Figure 4a](#) shows the change of T_{ov} with varying d_{oil} . We see that the temperature is up to 3.5 K lower in oil-poor regions than in oil-rich regions. In the following, we will theoretically examine the influence of this thickness-induced temperature difference on nucleation. According to the classical nucleation theory (CNT), water vapor molecules diffuse to the oil-

vapor interface and then form clusters which can grow only if their sizes exceed a critical size r_c . The heterogeneous nucleation rate density J ($\#/(m^2 \cdot s)$) can be calculated by [32]:

$$J = J_0 \exp\left(-\frac{\Delta G}{kT_{ov}}\right), \quad (3)$$

where J_0 is a kinetic pre-exponential factor, k is the Boltzmann constant, T_{ov} is the absolute temperature of the oil-vapor interface, and ΔG is the free-energy barrier corresponding to the critical nucleation radius r_c :

$$\Delta G = \gamma_{dv}A_{dv} + \gamma_{do}A_{do} - \gamma_{ov}\pi r_c^2 - (P_d - P_v)V_d. \quad (4)$$

In eq. (4), V_d is the volume of the nucleus, and $A_{i,j}$ are the interfacial areas between phases i and j , with the subscripts o, d, v, ov, do, and dv representing the oil, droplet, vapor, oil-vapor, droplet-oil, and droplet-vapor phases, respectively. $(P_d - P_v)$ is the Laplace pressure difference between vapor and droplet. As illustrated in the schematic of [Figure 4a](#), water vapor nucleates at the oil-vapor interface and the droplet can be approximated as two hemispherical caps with a deformation angle α_1 of the upper hemispherical cap and angle α_2 of the lower hemispherical cap. Hence, the interfacial areas A_{dv} , A_{do} , and the volume V_d can be described by [13,33]:

$$A_{dv} = 2\pi R_1^2(1 - \cos \alpha_1), \quad A_{do} = 2\pi R_2^2(1 - \cos \alpha_2), \quad (5)$$

$$V_d = \frac{\pi R_1^3}{3}[2 - \cos \alpha_1(2 + \sin^2 \alpha_1)] + \frac{\pi R_2^3}{3}[2 - \cos \alpha_2(2 + \sin^2 \alpha_2)], \quad (6)$$

where R_1 and R_2 are the equilibrium radii of upper and lower curvature, respectively, and can be obtained through $R_1 \sin \alpha_1 = R_2 \sin \alpha_2 = r_c$. The critical nucleation radius and the Laplace pressure difference $(P_d - P_v)$ can be estimated respectively using [34]:

$$r_c = \frac{2\gamma_{ov}}{(P_v - P_d)} \frac{\sin \alpha_1 \sin \alpha_2}{\sin(\alpha_1 + \alpha_2)}, \quad (7)$$

$$P_d - P_v = \frac{kT_{ov}}{V_{m,d}} \ln\left(\frac{P_v}{P_{sat}}\right), \quad (8)$$

where P_{sat} and $V_{m,d}$ represent the saturation pressure and liquid molar volume at the saturation pressure, respectively.

Since Krytox oils cloak water in our three-phase (oil-water-vapor) system, the Neumann triangle law collapses. To calculate the angles α_1 and α_2 , we modified the Neumann triangle equations by replacing the interfacial tension γ_{dv} with a combined effective surface tension γ_{eff} [29,35]:

$$\cos \alpha_1 = \cos(\pi - \theta_v) = \cos \theta_v = \frac{\gamma_{do}^2 - \gamma_{eff}^2 - \gamma_{ov}^2}{2\gamma_{ov}\gamma_{eff}}, \quad (9-1)$$

$$\cos \alpha_2 = \cos \theta_o = \frac{\gamma_{eff}^2 - \gamma_{ov}^2 - \gamma_{do}^2}{2\gamma_{do}\gamma_{ov}}. \quad (9-2)$$

With a measured value of $\theta_v \approx 150^\circ$ for the same material system [12], the value of γ_{eff} can be determined by eq. (9-1) to $\gamma_{eff} \approx 66$ mN/m. By combining eqs. (2) and (4) – (9), we can obtain the change of the free-energy barrier ΔG versus the oil film thickness d_{oil} (from oil-poor regions to oil-rich regions on LIS), corresponding to different temperatures T_{ov} , as seen in [Figure 4a](#). A bulk vapor temperature of $T_v = 303$ K was assumed in the calculation. We see that the energy barrier for nucleation is approximately one order of magnitude lower in oil-poor regions than in oil-rich regions, which confirms our hypothesis and initial observations that nucleation occurs predominantly in oil-poor regions.

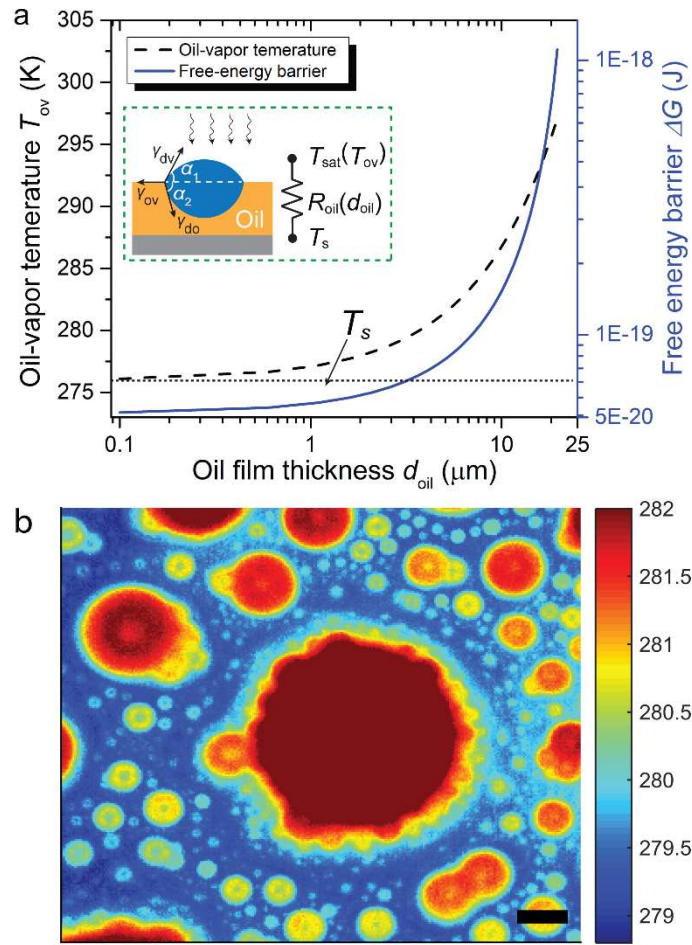


Figure 4 (a) Dependence of oil-vapor interfacial temperature T_{ov} and free energy ΔG on the oil film thickness d_{oil} . The calculation is based on the assumption of $T_s = 276$ K, $T_v = 303$ K and heat flux $q'' = 100$ kW/m². The inserted schematic shows the thermal path through the oil film with the conduction resistance R_{oil} . (b) Temperature distribution at the oil-vapor interface during condensation, obtained by the infrared imaging in top-view. The scale bar is 200 μm and the temperature scale is shown without calibration for a relative comparison only. Note that the temperature in the center of the large droplet is shown as saturated to focus on the temperature distribution of the oil.

To experimentally validate the calculation results, we used a Telops FAST M3k infrared camera equipped with a 4 \times lens (Telops) at a resolution of 7.5 $\mu\text{m}/\text{pixel}$ to measure the temperature distribution of the lubricant-vapor interface in top-view of a LIS sample during water condensation. Heat flows from the hot vapor to the cold copper block, which acts as a heat sink. As shown in **Figure 4b**, the surface temperature of the droplets are highest due to the size effect on the thermal resistance. Please note that the temperature in the center of the large droplet is shown as saturated to focus on the temperature distribution of the oil. Furthermore, note that the temperature readout has not been calibrated with respect to a blackbody radiation and serves for a relative comparison of interfacial temperatures only. In this scale, the “real” temperature of the large central droplet is approximately 285 K. The smaller the radius of a droplet, the lower its temperature. An obvious temperature gradient can be seen between oil-rich regions surrounding the droplets and oil-poor regions due to the reduction in oil film thickness, which agrees well with our calculation. Along with the higher temperature, oil-rich regions typically surround big droplets, and the big droplets will capture more water vapor molecules, lowering the chances of cluster formation in the oil-rich regions

due to vapor depletion in the gas mixture, supporting our hypothesis and observations on preferred nucleation in oil-poor regions. Similarly, this kind of “nucleation-free zone” is also reported in studies on dropwise condensation on partial/non-wetting solid surfaces [36]. It is worthy to note that nucleation is likely to occur at the oil-vapor interface in oil-rich regions only when the vapor supersaturation is sufficiently high. However, this nucleation in oil-rich regions is expected to be short lasting, as nucleation releases a large amount of latent heat, leading to a fast increase in the interfacial oil-vapor temperature.

3.2 Dynamics of oil-poor regions

Since oil-poor regions are favored for nucleation, the area ratio of oil-poor regions to the total surface is expected to affect the overall nucleation rate density and thereby heat transfer performances. Previously, we reported that the location and area-ratio of oil-rich and oil-poor regions tend to dynamically change because of continuous nucleation formation, growth and departure of condensed droplets caused by external forces during condensation. Hence, it is essential to quantitatively investigate how the area ratio of oil-poor regions changes over time. Also, the lubricant viscosity significantly affects the movement of condensate droplets and a higher frequency and velocity of droplet movement can be achieved by choosing a low-viscosity lubricant [12,31]. The dependence of the oil-poor regions on the lubricant viscosity is worthy of further examination. We conducted condensation experiments on horizontally placed samples with GPL 102 (73 cP) and GPL 106 (1627 cP) at $T_s \approx 273$ K and $T_v \approx 289$ K in an open environment. Videos were analyzed to obtain the area of oil-poor regions at different frames using ImageJ, as shown in [Figure 5a](#). Detailed information can be found in [Section 2.3](#). The first generation of nucleating droplets is uniformly spread on the surface and submerges into the oil film due to the cloaking tendency of Krytox. Continuous growth and coalescence of droplets pulls surrounding oil towards larger droplets or droplet clusters, forming the oil-rich regions, corresponding to the dark areas in [Figures 5b, c](#). In the meantime, oil-poor regions, that is, the bright area in the images, form due to the conservation of mass of the oil phase. The droplets grow faster on the LIS with low-viscosity lubricant owing to a shorter characteristic time of coalescence [25]. As shown in [Figure 5a](#), the oil-poor regions emerge much faster on the LIS with Krytox GPL 102 (lower viscosity), typically within 10 seconds of condensation, and the area of oil-poor regions quickly grows to 50% of the total surface, as a great amount of oil gathers around the rapidly growing droplets due to capillary effects. Then, this ratio gradually decreases to a quasi-steady value of about 21%, since more subsequent generations of nucleation occur in these oil-poor regions. For Krytox GPL 106 (higher viscosity), the coalescence of the initial small droplets takes significantly longer. A layer of ‘breath-figure’ water condensate droplets uniformly grow for nearly 40 seconds. Then, the breath-figure splits due to coalescence. The coalescence events will continuously create more oil-poor regions until the ratio stabilizes around 12% of the total surface area. Please note that these values are time-averaged, quasi-steady state values of the area ratio on the entire sample. The local oil-poor area might decrease to zero due to the occupancy of big droplets and then be renewed by cyclic sweeping events. For a solid hydrophobic surface, some studies reported that the droplet coverage typically reaches 60% of the total surface [36], but thin bands, *i.e.*, the nucleation-free zone, occur around existing drops as a result of limited vapor diffusion in the presence of non-condensable gases, hindered by the larger droplets. In our control experiments on the hydrophobic HTMS sample, the width of this nucleation-free zone was usually around 15 - 25 μm . Therefore, the effective available area for nucleation on hydrophobic surfaces will comprise approximately 15% of the total surface. Based on these findings, we hypothesize that the (re-)nucleation rate density is higher for lower viscosity oils due to a) a larger area-availability for nucleation, and b) higher droplet mobility, which can lead to more frequency re-nucleation on the same nucleation site.

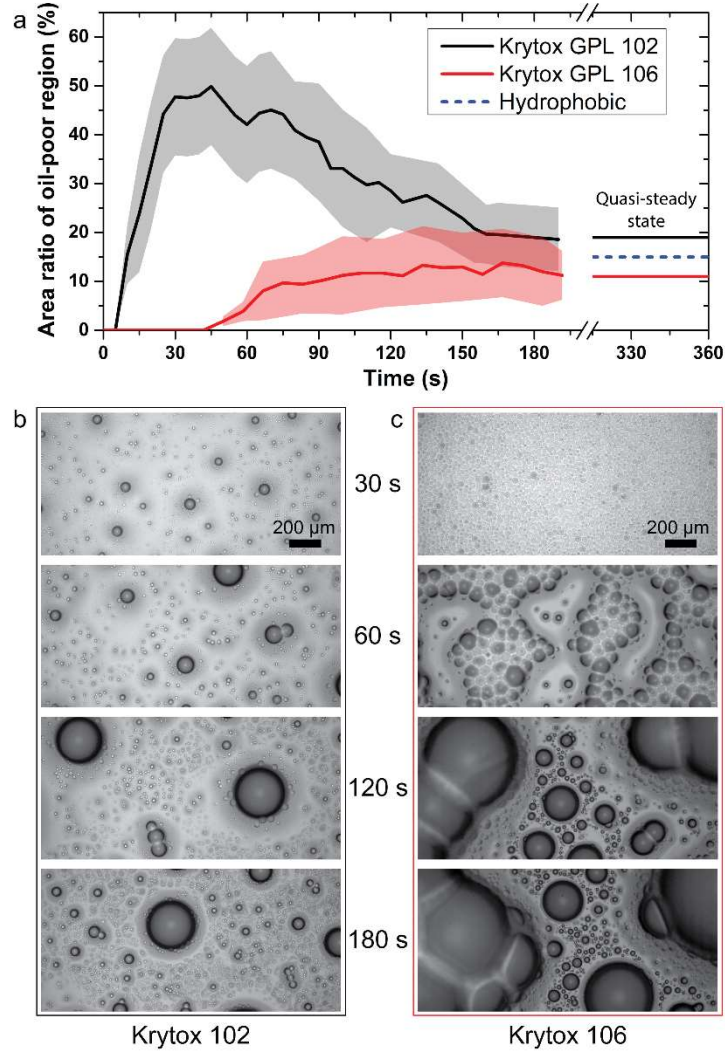


Figure 5 (a) Formation and time evolution of oil-poor regions on LIS infused with Krytox GPL 102 (73 cP) and Krytox GPL 106 (1627 cP) at $T_s \approx 273$ K and $T_v \approx 289$ K in an open environment, respectively. The shaded area represents the standard deviation of 17 individual experiments. The quasi-steady state, *i.e.*, long-term average area available for nucleation is also shown at larger times and compared to that of a solid hydrophobic surface [36]. (b) and (c) Snapshots of oil film dynamics at $t = 30$ s, 60 s, 120 s, and 180 s on LIS with (b) Krytox GPL 102 and (c) Krytox GPL 106.

3.3 Time evolution of nucleation rate density on LIS

Currently, models for the theoretical calculation of heat transfer rates during dropletwise condensation are based on an integration of the per-droplet heat transfer over the size distribution of droplets [19,37,38]. On LIS, the time-average condensate droplet size distribution shows no dependence on lubricant viscosity [39]. On the contrary, from experiments it was reported that lubricant-infused surfaces with oil of lower viscosity show a higher heat transfer coefficient and a larger volume of departure water droplets than those on LIS with higher oil viscosity [24]. We presume that the discrepancy is attributed to the dependence of the nucleation rate density on lubricant viscosity at the basis of the influence of lubricant viscosity on the area-availability for nucleation, *i.e.*, ratio of oil-poor regions. A high droplet nucleation rate density is key to enhancing the heat transfer rates, since nearly 75% of total heat transfer happens for droplets smaller than

10 μm [39]. Hence, a macroscopic condensate droplet size distribution seems to be inadequate to represent the real nucleation and heat transfer performance on LIS. To substantiate this claim, we first examined the nucleation rate density during a full natural sweeping cycle. **Figure 6a** shows that the nucleation rate density evolves with time during a sweeping cycle on a vertically placed LIS with Krytox GPL 104 at the temperatures $T_v \approx 304$ K and $T_s \approx 275$ K. Initially, the nucleation rate density increases sharply on the surface that was refreshed by a sweeping droplet under gravity at $t = 0$, as schematically shown in **Figure 6a-i**. After achieving a maximum value of 1.1×10^9 $\#/\text{m}^2\text{s}$ at $t \approx 12$ s (**Figure 6a-ii**), the nucleation rate density starts to slowly decrease due to a continuous accumulation of condensate droplets, which can be considered as a quasi-steady state, as shown in the schematic of **Figure 6a-iii**. Finally, the entire area is swept again by a large droplet rolling down the surface due to gravity, and the cycle begins from the top. During quasi-steady state, local coalescence events are able to boost the nucleation rate density. At around $t = 120$ s (**Figure 6a-iv**), for example, as two large droplets coalesce (the smaller one gets “swallowed” by its bigger neighbor) an oil ring is left behind, in which the oil thickness is unevenly distributed: an oil-poor region in the center and an oil-rich region along the periphery of the original droplet location, which spurs a transient sharp increase in the nucleation rate density. Although the time-averaged distribution of droplet sizes on LIS follows the model developed by Rose, we observed an unceasing high nucleation rate density on the LIS due to the high mobility of condensate droplets. For dropwise condensation on the hydrophobic surface, on the contrary, the nucleation rate density was intermittent due to random coalescence events.

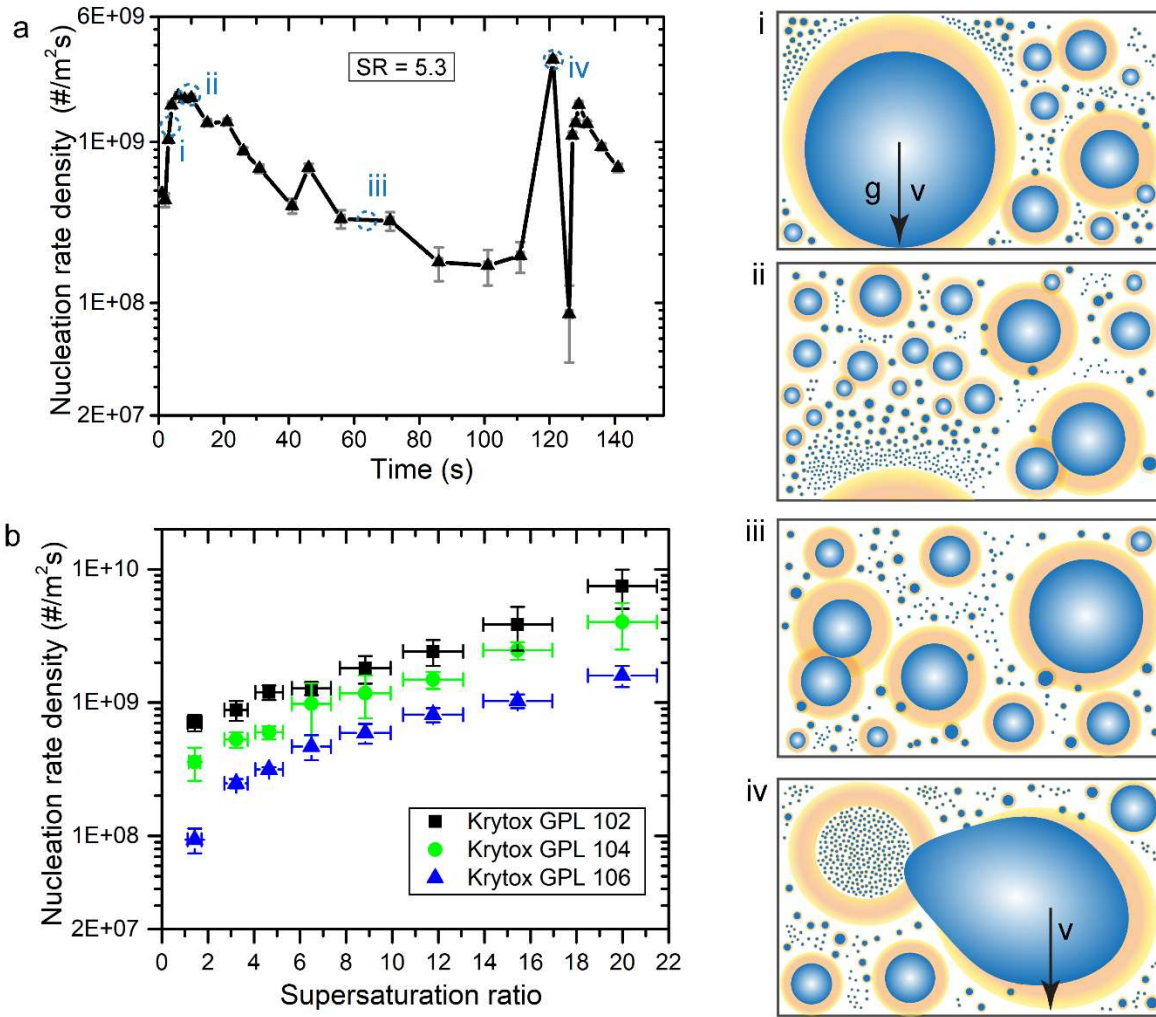


Figure 6 (a) The nucleation rate density (NRD) changes with time on a vertically placed LIS with Krytox GPL 104 at $T_v = 305$ K and $T_s = 276$ K (supersaturation $SR = 5.3$). The inserted schematics (i – iv) depict condensation dynamics on the LIS at different characteristic times during a condensation cycle, and are modeled after the actual videographic signature. (b) Dependence of nucleation rate density on lubricant viscosity at different supersaturation ratios. The horizontal error bars are from the fluctuation of vapor and substrate temperatures and the vertical error bars were determined from one standard error in the mean from experiments.

3.4 Effects of lubricant viscosity and supersaturation ratio on the nucleation rate density

Up to now, we have shown that nucleation mainly occurs in the oil-poor regions and that the area ratio of oil-poor regions can be further enhanced by lowering the lubricant viscosity. Therefore, we postulate that the nucleation rate density should differ for varying lubricant viscosities. To reveal the dependence of the nucleation rate density on lubricant viscosity, condensation experiments on LIS with Krytox GPL 102, 104, and 106 were conducted at a series of vapor temperatures, leading to a wide range of supersaturation ratios (SRs). On a vertically placed LIS, natural sweeping rates and maximum radii of droplets before being swept are a function of the vertical location on the substrate. To exclude the dependence of nucleation rate density on the substrate location, condensation experiments were conducted on horizontally placed LIS. We averaged the mean nucleation rate density from several full sweeping cycles at the respective experimental

settings (for more information, see [section 2.4](#)). The graph in [Figure 6b](#) shows that the nucleation rate density increases with SR for all lubricant viscosities, as expected, since the energy barrier for heterogeneous nucleation on the oil-vapor interface decreases with SR according to the classical nucleation theory [40]. Importantly, we also observe that the nucleation rate density shows a strong dependence on the lubricant viscosity. For example, a three-fold increase in nucleation rate density can be achieved by lowering the lubricant viscosity from 1627 cP to 73 cP.

We attribute the enhancement to the higher area-availability for nucleation and higher mobility of condensate droplets on LIS with lower lubricant viscosity (GPL 102). The total area of oil-poor regions, *i.e.*, preferable area for nucleation, is double on LIS with GPL 102 than on GPL 106 (see [section 3.2](#)). During condensation, we noticed condensate droplets of all sizes are ‘dancing’ on LIS with low-viscosity oil (GPL 102) and the high mobility has two distinct effects on the nucleation rate density. First, the frequent movements can effectively and continuously sweep the occupying droplets and leave fresh oil-poor regions behind their trajectories (compare to the schematic in [Figure 6a-iv](#)). Second, the movement can disturb the diffusion layer of the non-condensable gas nearby the lubricant-vapor interface [41]. In the following, we will separately discuss these two contributions.

As shown in [Figure 7a](#), condensate droplets (outlined by dashed cyan circles) typically move long distances along the dashed lines and leave behind a large area of oil-poor regions (highlighted by red ellipses), as shown here at intervals of ≈ 0.7 s on LIS with GPL 102. Subsequently, a high density of nucleation is observed. Before gravity comes into play, the microdroplets continuously sweep the condensed droplets, which frequently exposes the colder area—previously occupied by the big droplets—to hot vapor, effectively contributing to more nucleation. For LIS with GPL 106, on the contrary, the movement velocity is lower and the travel distances of moving droplets are much shorter, reducing the effective re-nucleation rate density.

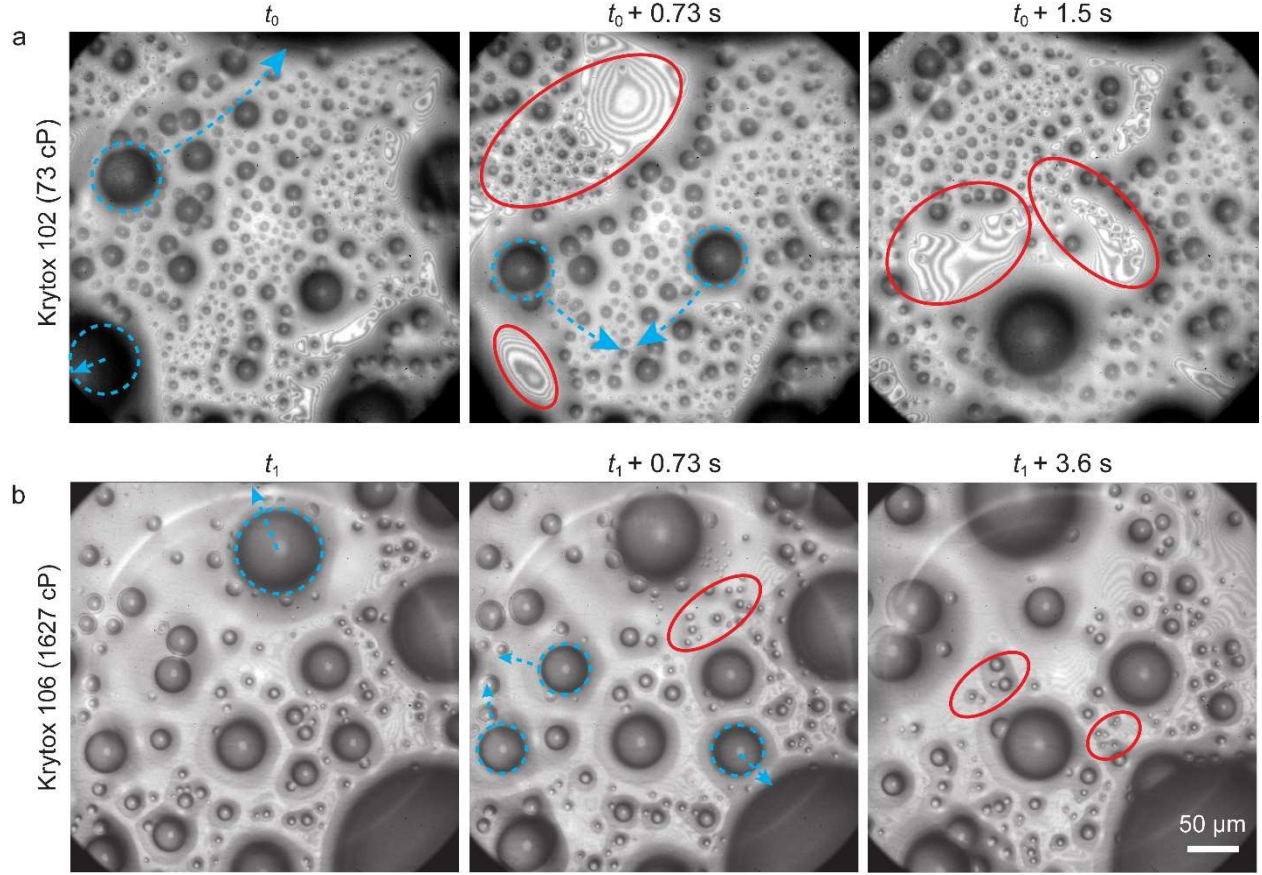


Figure 7 Image sequences of condensation on LIS with (a) Krytox GPL 102 and (b) Krytox GPL 106 at $T_v = 315$ K and $T_s = 276$ K. The initial times $t_0 = 59.2$ s and $t_1 = 45.2$ s represent the starting point of the 6th sweeping cycle. Cyan color arrow lines indicate the movement and direction of droplets highlighted by cyan dash circles and the red ellipses represent the oil-poor regions with re-nucleation.

In addition to directly clearing nucleation sites, rapid and frequent movement of droplets can potentially disturb the diffusion boundary layer of the non-condensable gas, which facilitates the diffusion of vapor to the oil-vapor interface. The non-condensable N_2 acts as carrier for water vapor to the environmental chamber in our experiments. During condensation, a thin non-condensable layer can build up near the oil-vapor interface and encompass the droplets. The accumulation of non-condensable gas not only hinders diffusion of water vapor molecules from the bulk gas-vapor mixture to the condensing surface, but also leads to a reduction in partial pressure of the vapor at the oil-vapor interface, leading to a decrease in saturation temperature. Overall, the nucleation rate density is restricted by the significant diffusion resistance of the non-condensable gas-vapor boundary layer for the oils of all viscosities [42,43].

To further support the hypothesis that the frequent and fast movement can disturb the diffusion layer, we approximate the thickness of this layer using a scaling analysis based on natural convection. Here, we treat the mixture of water vapor and N_2 as air (ideal gas) in the analysis, and assume that the non-condensable gas boundary layer thickness is on the same order as the vapor concentration boundary layer thickness δ_c . The transport of water molecules is dominated by diffusion rather than convection if the Peclet number $Pe_C = U\delta_c/D < 1$, where U is the velocity of the gas mixtures and D is the mass diffusion coefficient. Provided that the gas velocity is considered as parabolic near the sample surface, the boundary layer thickness σ_c can be estimated by letting $Pe_C = 1$ [44]:

$$\delta_c \sim \left[\frac{D\delta^{\frac{3}{2}}}{4(\beta g \Delta T)^{\frac{1}{2}}} \right]^{1/3}, \quad (10)$$

where $\Delta T = T_{ov} - T_s$, β is the volume thermal expansion coefficient of air, g is the gravitational acceleration, and the hydrodynamic boundary layer thickness $\delta \sim L \cdot Gr^{-1/5} = L \cdot \left(\frac{g\beta\Delta TL^3}{\nu^2} \right)^{-1/5}$, where Gr is the Grashof number, L is the characteristic length of the sample, $L \approx 25$ mm, and ν is the kinematic viscosity. Approximating the mixture as air, we use $\nu \approx 1.6 \times 10^{-5}$ m²/s, $\Delta T = 40$ K, and $\beta = 3.43 \times 10^{-3}$ / K. These values give $Gr \approx 81,000$ and $\delta \approx 2.6$ mm with the water vapor diffusion coefficient $D = 2.42 \times 10^{-5}$ m²/s at atmospheric pressure and room temperature. Hence, at $\Delta T = 40$ K, one finds $\delta_c \approx 0.88$ mm, which is on the same order as the size of the larger droplets. Therefore, the fast movement of big condensate droplets inside the diffusion layer is expected to disturb the diffusion layer of water vapor and enhance convective vapor transport to the oil-vapor interface.

4 Conclusions

In this work, we showed that nucleation is limited to the oil-poor regions and highly dependent on the lubricant viscosity. Using a 1D thermal conduction model through the oil film, we showed that the temperature at the oil-vapor interface is lower in the oil-poor regions than the oil-rich regions, which was also confirmed infrared imaging. Based on Gibbs' thermodynamics analysis, even a small temperature difference can significantly affect nucleation because of an exponential temperature dependence of the nucleation barrier energy. We also found that the area ratio of oil-poor regions dynamically changes with time. By lowering the lubricant viscosity from 1627 to 73 cP, we observed that the average area ratio of oil-poor regions increases from 12% to 21%. Then, we experimentally examined the dependence of the nucleation rate density on lubricant viscosity at a broad range of supersaturation ratios. The results showed the nucleation rate density is proportional to the supersaturation ratios, in agreement with the classical nucleation theory. At a given supersaturation ratio, higher nucleation rate densities could be achieved by lowering the lubricant viscosity. This increase can be attributed to a) a larger area available for re-nucleation, and b) a higher frequency and speed of condensate droplets of all sizes on LIS with lower viscosity Krytox oils. Microscale droplets spontaneously move towards relatively bigger droplets, that is, oil-rich regions. The robust movement can efficiently refresh the surface by sweeping all of droplets in the trajectories of the moving droplets and then leave an empty oil-poor region behind for new nucleation. At the same time, using scale analysis we argue that the movement can also disturb the non-condensable gas / vapor diffusion boundary layer and thereby enhance the nucleation rate density. The majority of nucleation rate density values reported in previous experimental studies were measured at the beginning of the condensation, whereas we demonstrate the importance of the re-nucleation rate density spanning a complete sweeping cycle. These findings could be helpful to comprehensively understand the interplay of the lubricant film and nucleation, and to enhance nucleation rate density and heat transfer performance by tailoring the lubricant viscosity.

Conflicts of interest

We report no conflicts of interest.

Acknowledgement

The authors would like to thank Michael Lorberg for assisting with droplet counting, and Jonathan Boreyko for elucidating discussions. The work was supported by the National Science Foundation, Grant No. 1856722. The authors acknowledge the use of instruments and staff assistance from the Institute of Materials Science and Engineering (IMSE), the Nano Research Facility (NRF), and the Jens Environmental Analysis Facility at Washington University in St. Louis.

References

- [1] L. Zhai, M.C. Berg, F.Ç. Cebeci, Y. Kim, J.M. Milwid, M.F. Rubner, R.E. Cohen, Patterned Superhydrophobic Surfaces: Toward a Synthetic Mimic of the Namib Desert Beetle, *Nano Lett.* 6 (2006) 1213–1217. <https://doi.org/10.1021/nl060644q>.
- [2] V.G. Reifert, A.I. Sardak, S.V. Grigorenko, V.L. Podbereznyj, Heat exchange at dropwise condensation in heat exchangers of desalination plants, *Desalination.* 74 (1989) 373–382. [https://doi.org/10.1016/0011-9164\(89\)85064-7](https://doi.org/10.1016/0011-9164(89)85064-7).
- [3] N. Lukic, L.L. Diezel, A.P. Fröba, A. Leipertz, Economical aspects of the improvement of a mechanical vapour compression desalination plant by dropwise condensation, *Desalination.* 264 (2010) 173–178. <https://doi.org/10.1016/j.desal.2010.07.023>.
- [4] R. Kehlhofer, *Combined-cycle Gas & Steam Turbine Power Plants*, PennWell Books, 1999.
- [5] N.A. Patankar, Supernucleating surfaces for nucleate boiling and dropwise condensation heat transfer, *Soft Matter.* 6 (2010) 1613–1620. <https://doi.org/10.1039/B923967G>.
- [6] R. Enright, N. Miljkovic, J.L. Alvarado, K. Kim, J.W. Rose, Dropwise Condensation on Micro- and Nanostructured Surfaces, *Nanoscale and Microscale Thermophysical Engineering.* 18 (2014) 223–250. <https://doi.org/10.1080/15567265.2013.862889>.
- [7] X. Chen, J. Wu, R. Ma, M. Hua, N. Koratkar, S. Yao, Z. Wang, Nanograsped Micropyramidal Architectures for Continuous Dropwise Condensation, *Adv. Funct. Mater.* 21 (2011) 4617–4623. <https://doi.org/10.1002/adfm.201101302>.
- [8] Y. Hou, M. Yu, X. Chen, Z. Wang, S. Yao, Recurrent Filmwise and Dropwise Condensation on a Beetle Mimetic Surface, *ACS Nano.* 9 (2015) 71–81. <https://doi.org/10.1021/nn505716b>.
- [9] T.-S. Wong, S.H. Kang, S.K.Y. Tang, E.J. Smythe, B.D. Hatton, A. Grinthal, J. Aizenberg, Bioinspired self-repairing slippery surfaces with pressure-stable omniphobicity, *Nature.* 477 (2011) 443–447. <https://doi.org/10.1038/nature10447>.
- [10] D.J. Preston, Z. Lu, Y. Song, Y. Zhao, K.L. Wilke, D.S. Antao, M. Louis, E.N. Wang, Heat Transfer Enhancement During Water and Hydrocarbon Condensation on Lubricant Infused Surfaces, *Scientific Reports.* 8 (2018) 1–9. <https://doi.org/10.1038/s41598-017-18955-x>.
- [11] M. Villegas, Y. Zhang, N. Abu Jarad, L. Soleymani, T.F. Didar, Liquid-Infused Surfaces: A Review of Theory, Design, and Applications, *ACS Nano.* 13 (2019) 8517–8536. <https://doi.org/10.1021/acsnano.9b04129>.
- [12] J. Sun, P.B. Weisensee, Microdroplet self-propulsion during dropwise condensation on lubricant-infused surfaces, *Soft Matter.* 15 (2019) 4808–4817. <https://doi.org/10.1039/C9SM00493A>.
- [13] F. Eslami, J.A.W. Elliott, Thermodynamic Investigation of the Barrier for Heterogeneous Nucleation on a Fluid Surface in Comparison with a Rigid Surface, *The Journal of Physical Chemistry B.* 115 (2011) 10646–10653. <https://doi.org/10.1021/jp202018e>.
- [14] L. Yang, X. Quan, P. Cheng, Z. Cheng, A free energy model and availability analysis for onset of condensation on rigid and liquid surfaces in moist air, *International Journal of Heat and Mass Transfer.* 78 (2014) 460–467. <https://doi.org/10.1016/j.ijheatmasstransfer.2014.07.006>.

- [15] M. Sokuler, G.K. Auernhammer, M. Roth, C. Liu, E. Bonaccorso, H.-J. Butt, The Softer the Better: Fast Condensation on Soft Surfaces, *Langmuir*. 26 (2010) 1544–1547. <https://doi.org/10.1021/la903996j>.
- [16] R. Xiao, N. Miljkovic, R. Enright, E.N. Wang, Immersion Condensation on Oil-Infused Heterogeneous Surfaces for Enhanced Heat Transfer, *Sci. Rep.* 3 (2013). <https://doi.org/10.1038/srep01988>.
- [17] S. Anand, A.T. Paxson, R. Dhiman, J.D. Smith, K.K. Varanasi, Enhanced Condensation on Lubricant-Impregnated Nanotextured Surfaces, *ACS Nano*. 6 (2012) 10122–10129. <https://doi.org/10.1021/nn303867y>.
- [18] X. Liu, P. Cheng, Dropwise condensation theory revisited: Part I. Droplet nucleation radius, *International Journal of Heat and Mass Transfer*. 83 (2015) 833–841. <https://doi.org/10.1016/j.ijheatmasstransfer.2014.11.009>.
- [19] P.B. Weisensee, Y. Wang, H. Qian, D. Schultz, W.P. King, N. Miljkovic, Condensate droplet size distribution on lubricant-infused surfaces, *International Journal of Heat and Mass Transfer*. 109 (2017) 187–199. <https://doi.org/10.1016/j.ijheatmasstransfer.2017.01.119>.
- [20] A. Kiselev, F. Bachmann, P. Pedevilla, S.J. Cox, A. Michaelides, D. Gerthsen, T. Leisner, Active sites in heterogeneous ice nucleation—the example of K-rich feldspars, *Science*. 355 (2017) 367–371. <https://doi.org/10.1126/science.aai8034>.
- [21] K.K. Varanasi, T. Deng, Controlling nucleation and growth of water using hybrid hydrophobic-hydrophilic surfaces, in: *IEEE*, 2010: pp. 1–5. <https://doi.org/10.1109/ITHERM.2010.5501324>.
- [22] S. Anand, K. Rykaczewski, S.B. Subramanyam, D. Beysens, K.K. Varanasi, How droplets nucleate and grow on liquids and liquid impregnated surfaces, *Soft Matter*. 11 (2015) 69–80. <https://doi.org/10.1039/C4SM01424C>.
- [23] T. Kajiya, F. Schellenberger, P. Papadopoulos, D. Vollmer, H.-J. Butt, 3D Imaging of Water-Drop Condensation on Hydrophobic and Hydrophilic Lubricant-Impregnated Surfaces, *Scientific Reports*. 6 (2016) 23687. <https://doi.org/10.1038/srep23687>.
- [24] H. Tsuchiya, M. Tenjimbayashi, T. Moriya, R. Yoshikawa, K. Sasaki, R. Togasawa, T. Yamazaki, K. Manabe, S. Shiratori, Liquid-Infused Smooth Surface for Improved Condensation Heat Transfer, *Langmuir*. 33 (2017) 8950–8960. <https://doi.org/10.1021/acs.langmuir.7b01991>.
- [25] J.B. Boreyko, G. Polyzos, P.G. Datskos, S.A. Sarles, C.P. Collier, Air-stable droplet interface bilayers on oil-infused surfaces, *Proceedings of the National Academy of Sciences*. 111 (2014) 7588–7593. <https://doi.org/10.1073/pnas.1400381111>.
- [26] A.G. Emslie, F.T. Bonner, L.G. Peck, Flow of a Viscous Liquid on a Rotating Disk, *Journal of Applied Physics*. 29 (1958) 858–862. <https://doi.org/10.1063/1.1723300>.
- [27] S. Anand, K. Rykaczewski, S.B. Subramanyam, D. Beysens, K.K. Varanasi, How droplets nucleate and grow on liquids and liquid impregnated surfaces, *Soft Matter*. 11 (2015) 69–80. <https://doi.org/10.1039/C4SM01424C>.
- [28] F. Schellenberger, J. Xie, N. Encinas, A. Hardy, M. Klapper, P. Papadopoulos, H.-J. Butt, D. Vollmer, Direct observation of drops on slippery lubricant-infused surfaces, *Soft Matter*. 11 (2015) 7617–7626. <https://doi.org/10.1039/C5SM01809A>.
- [29] M.J. Kreder, D. Daniel, A. Tetreault, Z. Cao, B. Lemaire, J.V.I. Timonen, J. Aizenberg, Film Dynamics and Lubricant Depletion by Droplets Moving on Lubricated Surfaces, *Phys. Rev. X*. 8 (2018) 031053. <https://doi.org/10.1103/PhysRevX.8.031053>.
- [30] D. Bonn, J. Eggers, J. Indekeu, J. Meunier, E. Rolley, Wetting and spreading, *Rev. Mod. Phys.* 81 (2009) 739–805. <https://doi.org/10.1103/RevModPhys.81.739>.
- [31] J.D. Smith, R. Dhiman, S. Anand, E. Reza-Garduno, R.E. Cohen, G.H. McKinley, K.K. Varanasi, Droplet mobility on lubricant-impregnated surfaces, *Soft Matter*. 9 (2013) 1772–1780. <https://doi.org/10.1039/C2SM27032C>.
- [32] A. Aleksandrov, B. Toshev, A. Sheludko, Nucleation from supersaturated water vapors on n-hexadecane: temperature dependence of critical supersaturation and line tension, *Langmuir*. 7 (1991) 3211–3215. <https://doi.org/10.1021/la00060a048>.

- [33] A.D. Alexandrov, B.V. Toshev, A.D. Scheludko, Nucleation from supersaturated water vapour on immiscible liquid substrates: Effect of the macroscopic geometry of the three-phase system on the critical supersaturation and the line tension, *Colloids and Surfaces A: Physicochemical and Engineering Aspects*. 79 (1993) 43–50. [https://doi.org/10.1016/0927-7757\(93\)80158-B](https://doi.org/10.1016/0927-7757(93)80158-B).
- [34] A.A. Nepomnyashchy, A.A. Golovin, A.E. Tikhomirova, V.A. Volpert, Nucleation and growth of droplets at a liquid-gas interface, *Phys. Rev. E*. 74 (2006) 021605. <https://doi.org/10.1103/PhysRevE.74.021605>.
- [35] C. Semprebon, G. McHale, H. Kusumaatmaja, Apparent contact angle and contact angle hysteresis on liquid infused surfaces, *Soft Matter*. 13 (2017) 101–110. <https://doi.org/10.1039/C6SM00920D>.
- [36] R.N. Leach, F. Stevens, S.C. Langford, J.T. Dickinson, Dropwise Condensation: Experiments and Simulations of Nucleation and Growth of Water Drops in a Cooling System, *Langmuir*. 22 (2006) 8864–8872. <https://doi.org/10.1021/la061901+>.
- [37] J.W. Rose, Dropwise condensation theory and experiment: A review, *Proceedings of the Institution of Mechanical Engineers, Part A: Journal of Power and Energy*. 216 (2002) 115–128. <https://doi.org/10.1243/09576500260049034>.
- [38] S. Kim, K.J. Kim, Dropwise Condensation Modeling Suitable for Superhydrophobic Surfaces, *J. Heat Transfer*. 133 (2011). <https://doi.org/10.1115/1.4003742>.
- [39] P.B. Weisensee, Y. Wang, H. Qian, D. Schultz, W.P. King, N. Miljkovic, Condensate droplet size distribution on lubricant-infused surfaces, *International Journal of Heat and Mass Transfer*. 109 (2017) 187–199. <https://doi.org/10.1016/j.ijheatmasstransfer.2017.01.119>.
- [40] D. Kashchiev, *Nucleation: Basic theory with applications*, Butterworth Heinemann, Oxford and Boston, 2000. <http://search.ebscohost.com/login.aspx?direct=true&scope=site&db=nlebk&db=nlabk&AN=207508>.
- [41] R. Wen, X. Zhou, B. Peng, Z. Lan, R. Yang, X. Ma, Falling-droplet-enhanced filmwise condensation in the presence of non-condensable gas, *International Journal of Heat and Mass Transfer*. 140 (2019) 173–186. <https://doi.org/10.1016/j.ijheatmasstransfer.2019.05.110>.
- [42] P.F. Peterson, V.E. Schrock, T. Kageyama, Diffusion Layer Theory for Turbulent Vapor Condensation With Noncondensable Gases, *J. Heat Transfer*. 115 (1993) 998–1003. <https://doi.org/10.1115/1.2911397>.
- [43] W.J. Minkowycz, E.M. Sparrow, Condensation heat transfer in the presence of noncondensables, interfacial resistance, superheating, variable properties, and diffusion, *International Journal of Heat and Mass Transfer*. 9 (1966) 1125–1144. [https://doi.org/10.1016/0017-9310\(66\)90035-4](https://doi.org/10.1016/0017-9310(66)90035-4).
- [44] M.-G. Medici, A. Mongruel, L. Royon, D. Beysens, Edge effects on water droplet condensation, *Phys. Rev. E*. 90 (2014) 062403. <https://doi.org/10.1103/PhysRevE.90.062403>.